

Final Progress Report

February 12, 2000 - February 11, 2001

ABSTRACT

The purpose of this investigation is to develop a new model for the acceleration of the fast solar wind by nonlinear, time-dependent multidimensional MHD simulations of waves in solar coronal holes. Computational studies indicate that nonlinear waves are generated in coronal holes by torsional Alfvén waves. These waves in addition to thermal conduction may contribute considerably to the accelerate the solar wind. Specific goals of this proposal are to investigate the generation of nonlinear solitary-like waves and their effect on solar wind acceleration by numerical 2.5D MHD simulation of coronal holes with a broad range of plasma and wave parameters; to study the effect of random disturbances at the base of a solar coronal hole on the fast solar wind acceleration with a more advanced 2.5D MHD model and to compare the results with the available observations; to extend the study to a full 3D MHD simulation of fast solar wind acceleration with a more realistic model of a coronal hole and solar boundary conditions. The ultimate goal of the three year study is to model the fast solar wind in a coronal hole, based on realistic boundary conditions in a coronal hole near the Sun, and the coronal hole structure (i.e., density, temperature, and magnetic field geometry) that will become available from the recently launched SOHO spacecraft. We report on our study of the effects of slow magnetosonic waves recently detected by EIT on the solar wind.

1. Introduction

The solar corona and the solar wind play a major role in determining the physical conditions of the interplanetary environment. However, the exact mechanism that energizes the solar coronal plasma and the solar wind is poorly understood. To study the physics of the multi-species plasma in the inner corona (the region where most of the heating and acceleration takes place) we use the multi-fluid description, applicable close to the sun. This is the first multi-fluid, multi-dimensional study of the solar wind that includes the self-consistent effects of MHD waves in a model coronal hole near the sun.

Recent Solar and Heliospheric (SOHO) Ultraviolet Coronagraph Spectrometer (UVCS) observations show that the physical properties of the minor ions in the corona provide clues

on the coronal heating and solar wind acceleration mechanism. UVCS observations suggest that protons reach 3.5×10^6 K within several solar radii, and O^{5+} and other minor ions exceed temperatures of 10^7 K in coronal holes (Kohl et al. 1997).

Low and high frequency Alfvén waves appear to be the best candidates for coronal heating in open magnetic structures, such as coronal hole. The frequency of these waves determines the microphysics of the heating process. The low frequency ($10^{-4} - 10^{-3}$ Hz) Alfvén waves can accelerate the solar wind by momentum transfer (first proposed by Alazraki & Courtier 1971, and Belcher 1971), and can heat the corona by viscous and resistive dissipation (first discussed by Barnes 1969). High frequency Alfvén waves (i.e., $10-10^4$ Hz range) will lead to the ion-cyclotron resonance which can preferentially heat the minor ions (e.g., Dusenbery & Hollweg 1981, McKenzie & Marsch 1982), and was proposed as the heating and the acceleration of the solar wind (e.g., Axford & McKenzie 1992). However, it is not clear whether there is sufficient energy in the high frequency Alfvén waves to account for heating of protons, and whether these waves can carry the energy from the magnetic network sufficiently high into the corona (e.g., Cranmer, Field, & Kohl 1999).

Recently, using the two-fluid 2.5D model we have shown that unresolved wave motion may account for the enhanced proton temperatures observed by UVCS (Ofman & Davila 1999, Davila & Ofman 1999). However, the self-consistent effect of waves on the minor ions has not been considered. In the present study we use three-fluid electron-proton-ion plasma with a broad band Alfvén waves source in the millihertz frequency range and include the effects of Coulomb friction, important for minor ions. We consider the self-consistent effect of waves on the observed line width temperatures of protons and O^{5+} ions in a structured coronal hole. The results of this study are relevant for the future *Solar Probe* mission, that will measure the plasma properties near the Sun (Sittler et al 1997).

UVCS observations indicate that O^{5+} ions and other minor ions exceed temperatures of 10^7 K in coronal holes, and in streamers (Kohl et al. 1997). The UVCS observations show a striking difference in the appearance of coronal streamers in minor ion emission lines compared to hydrogen UV emission. These observations show that the emission from O^{5+} ions is stronger by an order of magnitude at the legs of streamers than in the central core of streamers (Figure 1). However, the brightness of the Ly- α emission peaks in the central core of streamers (Kohl et al. 1997, Raymond et al. 1997a).

Several possibilities which can explain the observed difference in the O^{5+} emission and Ly- α in streamers are discussed by Noci et al. (1997). One of Noci et al. (1997) suggestions is that variation of minor ion abundance (i.e., ion density relative to proton density) may occur due to Coulomb friction with outflowing protons (Geiss, Hirt, & Entwyler 1970) in a double-streamer geometry. Noci et al. (1997) concludes that only an abundance variation

of O^{5+} across the streamer is consistent with the observations of other minor ion emissions in streamers, such as Mg^{9+} (625Å), Si^{6+} (499Å), and Fe^{11+} (1242Å). Raymond et al. (1997a, b) suggested that gravitational settling in the core of streamers is the dominant mechanism for the depletion of O^{5+} there. However, the 1D single-fluid time-dependent model of the settling and diffusion of ions in the streamer core predicts that the abundance in the streamer legs is less than in the core of the streamer, in conflict with observations (Raymond et al. 1997b).

Early computational models of O^{5+} ions in the solar wind did not include the full ion dynamics and treated the O^{5+} ions as test particles in one-dimensional solar wind flow (Geiss, Hirt, & Entwyler 1970, Joselyn & Holzer 1978, Bürgi & Geiss 1986, Esser & Leer 1990). More recent multi-fluid studies of the flow of O^{5+} ions in the solar wind were confined to one spatial dimension (Li et al 1997, Raymond et al. 1997b). Although these models made important contribution to our understanding of the minor-ion dynamics in the solar wind, the effects of coronal magnetic and density structure due to streamers were not included self-consistently.

Ion-cyclotron waves were suggested as the source of energy for the heating and the acceleration of the solar wind. There are various mechanisms that can generate ion-cyclotron waves in a plasma (e.g. ion temperature anisotropy, ion beams, etc.). However the dominant mechanism and its source for the generation of these high frequency waves in the solar corona is not well understood. If these waves are present, their direct signature could be detected in the future *Solar Probe* mission, that will measure in-situ plasma properties close to the Sun (Sittler et al 1997).

It has been suggested that the observed O^{5+} temperature anisotropy is the result of ion-cyclotron heating by the appropriate power-law spectrum of ion-cyclotron waves generated lower in the corona (Cranmer, Field, & Kohl 1999). Cranmer et al. (1999) reports that the most probable perpendicular O^{5+} speed is more than an order of magnitude larger than the most probable parallel speed at $3.5R_{\odot}$. Due to the long integration time (several hours) of the UVCS observations and the line-of-sight contribution of several solar radii to the observed emission the observed velocity distributions are likely to contain both microscopic and macroscopic motions. The macroscopic motions may be due to unresolved magnetohydrodynamic (MHD) turbulence or low frequency MHD wave motions (Ofman & Davila 1997a).

2. Three-Fluid 2.5D MHD Model Equations

To investigate the dynamics of protons and O^{5+} ions in the solar wind we solve the three-fluid MHD equations with full ion dynamics (Braginskii 1965) in spherical geometry. The 2.5D equations are obtained by taking $\partial/\partial\phi = 0$ in the 3D three-fluid MHD equations, i.e., by assuming azimuthal symmetry, and keeping all three components of the species velocities and fields.

In the model we neglect electron inertia (since $m_e \ll m_p$, where m_e is the electron mass and m_p is the ion mass), relativistic effects ($V \ll c$), and assume quasi-neutrality of the plasma ($n_e = n_p + Zn_i$, where n_e is the electron density, n_p is the proton density, n_i is the ion density, and Z is the charge state of the ions). We neglect the ion-cyclotron terms since the relevant time scales are orders of magnitude larger than the ion gyro-period.

The normalized three-fluid MHD equations are

$$\frac{\partial n_k}{\partial t} + \nabla \cdot (n_k \mathbf{V}_k) = 0, \quad (1)$$

$$n_k \left[\frac{\partial \mathbf{V}_k}{\partial t} + (\mathbf{V}_k \cdot \nabla) \mathbf{V}_k \right] = -E_k \nabla p_k - E_e \frac{Z_k n_k}{A_k n_e} \nabla p_e - \frac{n_k}{F_r r^2} + Z_k a_k \frac{n_k}{n_e} (\nabla \times \mathbf{B}) \times \mathbf{B} + \mathbf{F}_{k.coul}, \quad (2)$$

$$\frac{\partial \mathbf{B}}{\partial t} = -\nabla \times \mathbf{E}, \quad \mathbf{E} = -\mathbf{V}_e \times \mathbf{B} + \frac{1}{S} \nabla \times \mathbf{B} \quad (3)$$

$$\mathbf{V}_e = \frac{1}{n_e} (n_p \mathbf{V}_p + Zn_i \mathbf{V}_i - b \nabla \times \mathbf{B}), \quad (4)$$

$$\frac{\partial T_k}{\partial t} = -(\gamma_k - 1) T_k \nabla \cdot \mathbf{V}_k - \mathbf{V}_k \cdot \nabla T_k, \quad (5)$$

where the index $k = p, i$. (in Equation (5) $k = e, p, i$), and p is protons, i is ions, and e is electrons. In the present model we assume that the corona is nearly isothermal (i.e., $\gamma_k \approx 1$), do not include heat sources explicitly, and neglect the thermal forces in the momentum equations. The viscous forces assumed to be negligible. We also neglected a temperature equilibration term in the energy equation due to heat transfer between the fluids, since observations show that the O^{5+} temperature remains higher than the proton and electron temperature, and the protons will not be heated significantly by the O^{5+} due to the small abundance of these ions. In the above equations the Coulomb friction terms $\mathbf{F}_{k.coul}$ can be found in Braginskii (1965). Note, that qualitatively the Coulomb friction increases with the velocity difference between the species, and with the density. The friction decreases when the temperature is increased.

We have used the following normalization: $r \rightarrow r/R_\odot$, where R_\odot is the solar

radius: $t \rightarrow t/\tau_A$; $V \rightarrow V/V_A$; $B \rightarrow B/B_0$; $n_{i,e,p} \rightarrow n_{i,e,p}/n_{e0}$; $S = \tau_r/\tau_A$ the Lundquist number: $\tau_r = 4\pi R_\odot^2/\nu c^2$ the resistive time scale, where ν is the resistivity, and c is the speed of light: $\tau_A = R_\odot/V_A$ the Alfvén time scale: V_A is the single-fluid Alfvén speed: $E_{e,p} = (k_b T_{e,p,0}/m_p)/V_A^2$ the electron or proton Euler number: $E_i = (k_b T_{i,0}/m_i)/V_A^2$ the ion Euler number: $F_r = V_A^2 R_\odot/(GM_\odot)$ the Froude number, where G is the universal gravitational constant and M_\odot is the solar mass; and the normalization constants $a_k = n_{p0}/n_{e0}/A_k + m_e/m_k + A_k n_{i0}/n_{e0}$; $b = cB_0/(4\pi e n_{e0} R_\odot V_A)$, where A_k is the atomic mass of each species, and Z_k is the charge state.

We have used the following parameters in the three-fluid model of streamers: the proton temperature $T_{p0} = 1.6 \times 10^6$ K; the electron temperature $T_{e0} = 1.6 \times 10^6$ K; the O^{5+} temperature $T_{O^{5+0}} = 12 \times 10^6$ K; the electron density $n_{e0} = 10^8$ cm $^{-3}$; and the O^{5+} density $n_{i0} = 6.2 \times 10^4$ cm $^{-3}$; the magnetic field $B_0 = 2$ G. These parameters are consistent with recent UVCS observations of streamers (Kohl et al. 1997, Li et al. 1998). Due to numerical limitations the O^{5+} temperature that we used is larger than the typical O^{5+} temperature ($\sim 5 \times 10^6$) estimated for a coronal streamer. For the above temperatures the proton scale height is $0.14R_\odot$ and the O^{5+} scale height is $0.039R_\odot$. Lower O^{5+} temperature results in smaller ion scale height, and nearly zero O^{5+} density in the core of a streamer that poses a numerical challenge beyond the scope of this study. However, since the Coulomb friction increases for lower O^{5+} temperature the results reported below should hold for $T_{O^{5+0}} = 5 \times 10^6$ K.

To initiate the modeling of the coronal streamer we have used the quadrupole field given by $\mathbf{B} = B_0 r^{-4}[(1 - 3 \cos^2 \theta)\mathbf{e}_r - \sin 2\theta \mathbf{e}_\theta]$. The initial proton density and outflow was uniform in θ and given by Parker's (Parker 1963) isothermal solution in r . The initial ion density was taken to be gravitationally stratified (with the gravitational acceleration corrected for the self consistent parallel electric field Raymond et al. 1997b), and uniform in θ . The initial uniform density at $r = 1R_\odot$ was chosen to isolate the latitudinal density variations generated by the magnetic configuration above the limb as the simulation evolves to the steady state. The arbitrary initial state is chosen in order to reach the steady state solution in a reasonable computational time. The boundary conditions were imposed at $r = 1R_\odot$, with $V_{k,r} \geq 0$ ($k = p, i$), and with incoming characteristics approximated by zero order extrapolation. At $r = r_{max}$, we have allowed for an outflow, and at $\theta = \pi/2, \pi$ we imposed $V_{k,\theta} = B_\theta = 0$, consistent with the quadrupole field geometry. The emphasis of this study is the slow solar wind, therefore, we did not include any additional sources of momentum or heating (such as waves) to produce the fast solar wind.

3. Slow solar Wind in Coronal Streamers: Numerical Results

We solved the above equations explicitly with the fourth-order Runge-Kutta type method in time, and fourth order differencing in space with 160×500 grid cells ($\delta\theta = 0.01$, $\delta r = 0.01$). A fourth order smoothing term was applied for stability. Two-fluid versions of this numerical approach have been used successfully for the modeling of the solar wind flow in coronal holes (Ofman & Davila 1999).

The results of the calculations with the three-fluid code are shown in Figure 2 for the UVCS field of view. The model was run until a streamer with the appropriate sheet current was formed and reached a steady state. The current sheet has a finite thickness and is resolved in the code (the Lundquist number was set to 10^5). The streamer proton density structure and magnetic field structure is in agreement with the single fluid streamer models (Pneuman, & Kopp 1971, Steinolfson, Suess, & Wu 1982, Washimi, Yoshino, & Ogino 1987, Cuperman, Ofman, & Dryer, 1990, Wang et al. 1993). The spatial variations of the proton density δn_p , and the O^{5+} density δn_i of a model coronal streamer at $t = 16$ hours are shown in Figure 2.

It is evident that the O^{5+} density is enhanced in the open field line regions of the streamer compared to the core, and the proton density is larger in the core of the streamer. The density enhancement at the close field boundary of the streamer is due to the compression by the Lorentz force due to the current sheet, calculated self-consistently in the model (the current sheet and the corresponding density enhancement is below resolution of present coronal observations). The proton density reached a steady state. The qualitative agreement between the model calculations of the proton and ion density structure, and the UVCS observations in Figure 1 is evident. Note, that in Figure 2 we model a streamer belt, while in Figure 1 the streamer is probably more localized in the longitudinal direction. Thus, 3D structure combined with line-of-sight integration of the observed O^{5+} emission of the ‘‘hollow’’ streamer may produce more localized legs.

In the top panel of Figure 3 we show the magnetic field line vectors of the model streamer. The length of the streamline vectors represent the intensity of the magnetic field. The field lines are closed in the core of the streamer. The self consistent streamer field with current sheets results from the time-dependent 2.5D three-fluid calculation. The velocity streamlines are shown in the bottom panel. In the core of the streamer there is small downflow of O^{5+} ions ($\sim 20 \text{ km s}^{-1}$), and no significant proton flow. Outside the core the flow is along the open field lines. The radial distance of the streamer cusp is determined by the magnetic field strength, geometry, and the plasma pressure (as in the single fluid models).

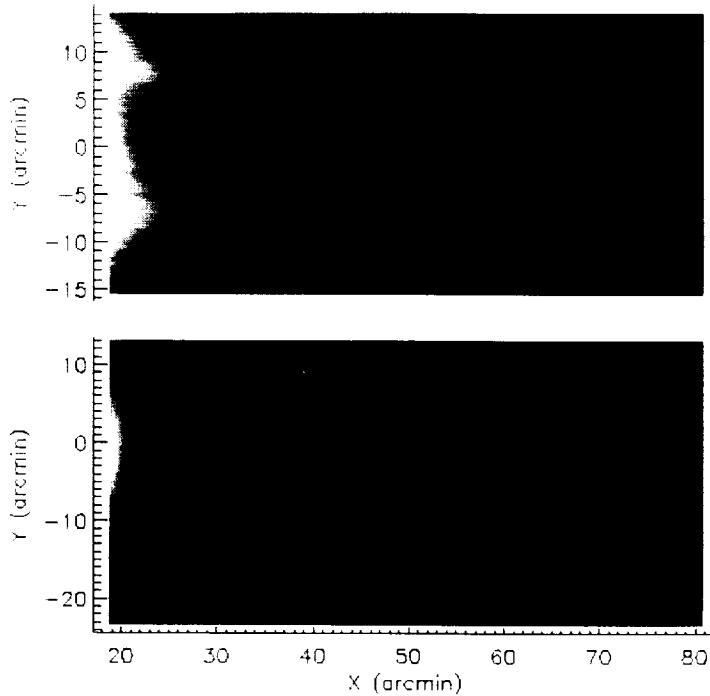


Fig. 1. --- Images of the UVCS 12 October 1996 observation of an equatorial streamer above the west limb in O^{5+} (top panel) and in Lyman- α (bottom panel) EUV emissions. The spatial scales are solar coordinates in arc min where the origin is at the center of the disk (Courtesy of SOHO/UVCS consortium. SOHO is a project of international cooperation between ESA and NASA).

In the top panel of Figure 4 we show the θ -dependence of the radial velocity of ions (solid lines) and protons (dashed lines) at $1.8R_{\odot}$ (thick lines) and $5R_{\odot}$ (thin lines). Outside the streamer core it is evident that the outflow velocity of O^{5+} is close to the outflow velocity of the protons. In the model we find that the outflow velocity is higher in the right leg of the streamer than in the left leg due to the asymmetry of the initial quadrupole field and the corresponding boundary conditions on the field at $r = 1R_{\odot}$. The magnitude of the outflow speed in the open field regions is in agreement with the outflow velocity for the slow solar wind deduced from UVCS observations using the Doppler dimming effect at this height (Strachan et al. 2000).

In the bottom panel of Figure 4 we show the θ -dependence of the proton and O^{5+} density. The O^{5+} abundance at the legs shows an order of magnitude enhancement compared to the core, in good agreement with the observations reported by Raymond et al. (1997a). The density spikes at the core boundaries are due to pressure balance with the

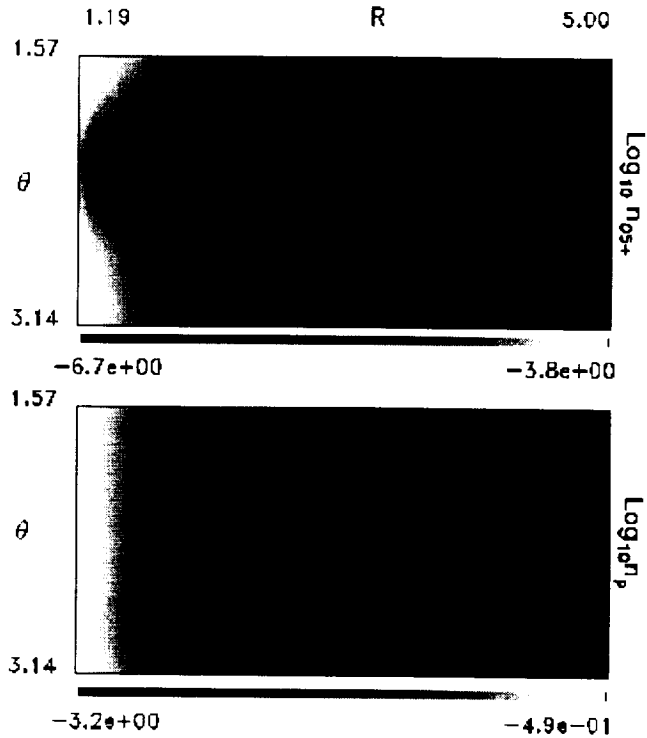


Fig. 2. -- The spatial variations of the O^{5+} (top panel) and proton (bottom panel) densities in the model coronal streamer at $t = 16$ hours.

current-sheet. They are not observed by UVCS, since the thickness of the current sheet is below resolution. The correlation between the outflow velocity, and the O^{5+} density is due to the effect of the Coulomb friction. The main differences in the detail between the model and observations stem from the difference in magnetic topology of the model streamer and the observed coronal streamer, and the possible latitudinal variation of the coronal density and temperature at the coronal boundary.

4. Low-frequency MHD waves in solar coronal holes: Initial conditions, boundary conditions, and driver

To model the dynamics of low-frequency MHD waves in the three-component plasma we use the following typical parameters: $\gamma_p = 1.05$, $\gamma_e = 1.05$, $\gamma_{O^{5+}} = 1.0$. $T_{p0} = 2 \times 10^6$ K, $T_{O^{5+}0} = 12 \times 10^6$ K, $T_{e0} = 0.8 \times 10^6$ K, $n_{e0} = 10^8$ cm $^{-3}$, $n_{O^{5+}0} = 8 \times 10^4$ cm $^{-3}$. $S = 10^4$,

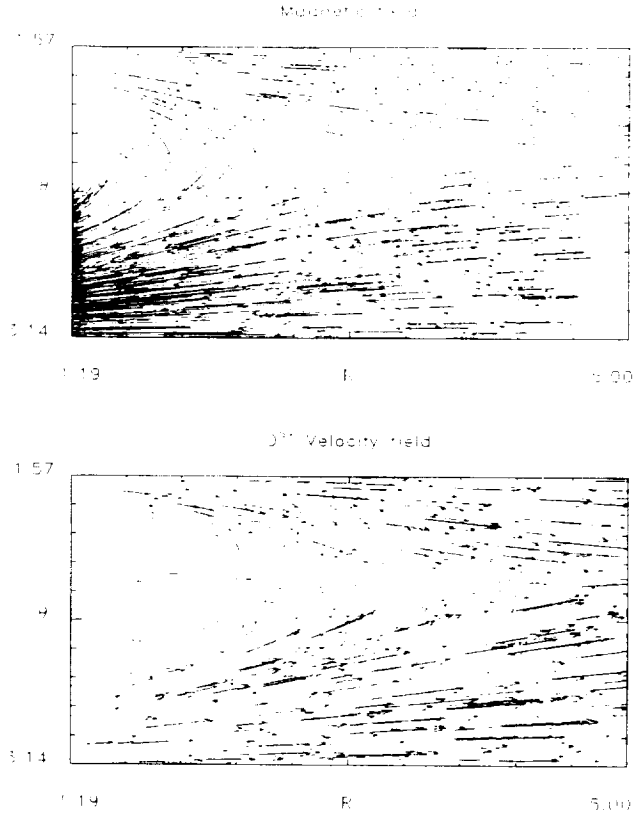


Fig. 3.— The magnetic field scaled by the square root of the total density (top panel) and the O^{5+} velocity field (bottom panel) of the model coronal streamer at the time shown in Figure 1. The longest velocity vectors correspond to 144 km s^{-1} flows, and the longest magnetic field vector correspond to 2.6 G .

$B_0 = 7 \text{ G}$ which gives $V_A = 1521 \text{ km s}^{-1}$. The abundance of O^{5+} relative to protons in the corona is about 8×10^{-6} (Wimmer-Schweingruber et al. 1998). Due to numerical limitations we are using a higher abundance of 8×10^{-4} that is consistent with the photospheric abundance of oxygen relative to hydrogen (Anders & Grevesse 1989). However, this has no significant effect on the results, since the dynamics of electrons and protons is not significantly affected by the minor ions. The initial densities of the protons, ions, and electrons are (see Figure 5)

$$n_{p0}(\theta, r) = \left[1 - (1 - n_r) e^{-[(\theta - \pi/2)/\theta_c]^4} \right] n_{p1D}(r)/n_r, \quad (6)$$

$$n_{i0}(\theta, r) = n_{p0}(\theta, 1)n_{i1D}(r), \quad (7)$$

$$n_{e0}(\theta, r) = n_{p0}(\theta, r) + Zn_{i0}(\theta, r). \quad (8)$$

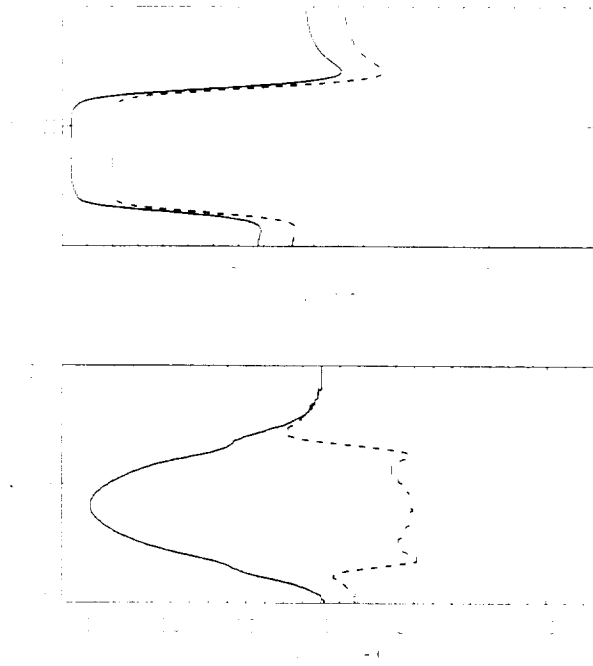


Fig. 4.— The θ -dependence of the velocity and the density at $r = 1.8R_{\odot}$ (thick lines) and $r = 5R_{\odot}$ (thin lines) for the model in Figure 1. The densities are scaled by the values at $\theta = \pi$. Solid lines are for O^{5+} , and the dashed lines are for protons.

where $n_r = 0.3$, the width of the low density region $\theta_c = 0.2$. The 1D densities $n_{p1D}(r)$, n_{i1D} and velocities used to initialize the 2.5D calculations are obtained from the polytropic steady state solution of the 1D version of the code.

The boundary conditions at $r = 1R_{\odot}$ are incoming characteristics approximated by zero order extrapolation.

$$B_r(1, \theta) = B_{r,0}, \quad V_{k,\theta} = B_{\theta} = 0, \quad T_p = T_{p0}, \quad T_e = T_{e0}, \quad T_i = T_{i0}. \quad (9)$$

At $r = r_{max}$, and at $\theta = \theta_{max}$ we use open boundary conditions, with symmetry boundary conditions imposed at $\theta = \pi/2$.

The broad band Alfvén wave driver is modeled by

$$B_{\phi}(t, \theta, r = 1) = -V_d/V_{A,r} F(t, \theta) \quad (10)$$

$$F(t, \theta) = \sum_{i=1}^N a_i \sin(\omega_i t + \Gamma_i(\theta)) \quad (11)$$

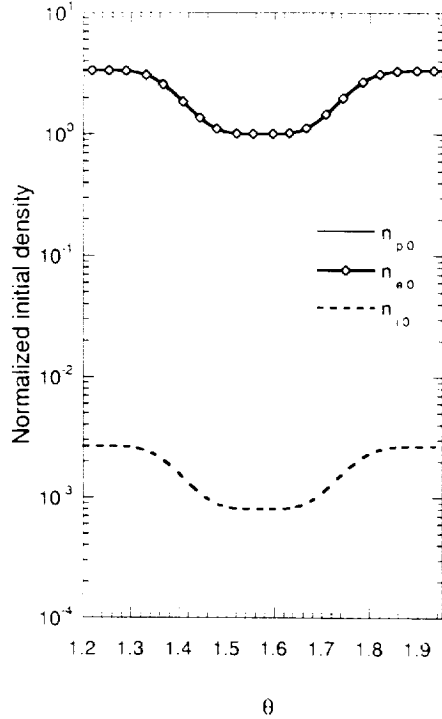


Fig. 5.— The initial density profile of the protons, electrons, and O^{5+} ions in the model coronal hole. Note, that the electron and proton densities are nearly identical. The densities are scaled by 10^8 cm^{-3} .

where $a_i = i^{-1/2}$, $\omega_i = \omega_1 + (i - 1)\Delta\omega$, $\Delta\omega = (\omega_N - \omega_1)/(N - 1)$, and $\Gamma_i(\theta)$ is the random phase, and N is the number of modes. The frequencies in the broad band driver are in the millihertz range $[\omega_0, \omega_N]$. In the present study we use $V_d = 0.015V_A$, $\omega_0 = 0.013 \text{ Rad s}^{-1}$, $\omega_N = 10\omega_0$, and $N = 100$. The coronal boundary is divided into eight regions that produce the Alfvén waves with a different $\Gamma_i(\theta)$.

4.1. Simulated emission line profile

The calibrated observed line profile is usually given in terms of radiative intensity as a function of wavelength. In order to convert the wavelength to velocity the Doppler's shift relation is used

$$\frac{\Delta\lambda}{\lambda_0} = \frac{v}{C}, \quad (12)$$

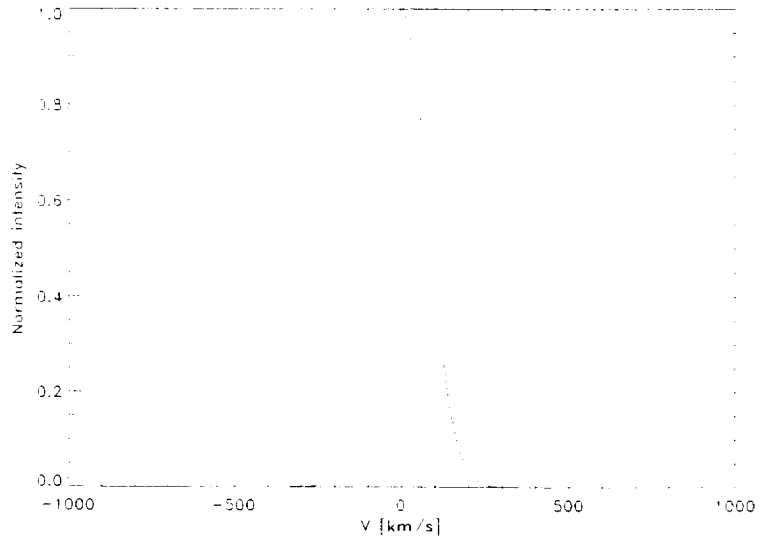


Fig. 6.— The thermal (solid line) and simulated (dashes) line profile at $4R_{\odot}$. The integration time is 1.7 hours.

where λ_0 is the wavelength of the peak intensity of the emission line, v is the line of sight velocity, and $\Delta\lambda$ is the wavelength shift due to the Doppler effect.

The simulated line intensity is obtained by integrating the thermal emission shifted by the nonthermal wave velocity $w(t)$ for the duration τ (typically several hours) of the simulated observation and over the line of sight s :

$$I(v) = \int_s \int_0^{\tau} \rho e^{-(v-w(t))^2/v_{\theta}^2} dt ds, \quad (13)$$

where v_{θ} is the kinetic thermal speed of the particles, and the emission is weighted by the density of the species for the resonantly scattered line. In the present study we assumed that the line of sight contribution comes from about ± 10 degree wedge in the center of the coronal hole. The effective temperature is obtained by determining the $v_{1/e}$ of the simulated line width broadened by the nonthermal motion. An example of a simulated emission line profile broadened by nonthermal wave motions at $4R_{\odot}$ integrated over 1.7 hours is shown in Figure 6.

5. Waves in solar coronal holes: Numerical Results

In Figure 7 we show the spatial dependence of the solutions at $t = 109\tau_A = 13.9$ hours. The ϕ -component of the proton and ion velocity, the Ohmic heating associated with the broad band Alfvén waves, and the radial velocity of the protons are shown in the $\theta - r$ plane. It is evident that the Alfvénic fluctuations propagate into the coronal hole in protons and ions. We found that the ratio of the proton wave amplitude and the ion wave amplitude is about $3.2 = A/Z$. This is expected from the ratio of the Lorenz forces exerted on the protons and on the ions in the momentum equation. It is also evident that the regions of largest Ohmic heating are associated with the highest amplitude Alfvén waves, with phase mixing effects at the boundary between the low and high density regions of the coronal hole.

The radial component of the proton velocity exhibits compressional fluctuations due to the nonlinear effects of the Alfvén wave pressure, in agreement with single fluid models (Ofman & Davila 1997b, Ofman & Davila 1998). On average, largest radial velocity occurs in regions of highest Alfvén wave amplitude. The radial velocity amplitude predicted by the model at $3R_\odot$ is about half the velocity deduced from UVCS observations at this height (Antonucci 1999). However, as Antonucci (1999) points out "...this velocity diagnostic depends critically on the modeling of the coronal properties along that line (line of sight)..." Thus, the reason for this discrepancy may be due to the choice of the magnetic field topology (i.e., divergence), Alfvén wave spectrum that affects the acceleration profile, and the other coronal parameters. Single fluid studies show that low frequency waves (<1 mHz) are needed to obtain the fast solar wind in coronal holes (Ofman & Davila 1998). However these low frequency waves accelerate the solar wind to fast wind speed beyond $10R_\odot$.

The future *Solar Probe* mission will approach the sun to $4R_\odot$, and will be able to measure the variations in the particle velocities *in-situ*. To show how these variations may look we plot in Figures 8-10 the temporal evolution of the V_r and V_ϕ of protons (top panel) and O^{5+} ions (bottom panel). The location is $r = 4R_\odot$ at $\theta = 1.58$ (solid line), 1.67 (short dashes), 1.76 (dashes), 1.85 (dot-dashes), 1.95 (3-dot-dashes). The velocities are scaled by the Alfvén speed $V_A = 1521 \text{ km s}^{-1}$, and the time is scaled by the Alfvén time, $\tau_A = 460 \text{ s}$.

It is evident that the variations of V_ϕ of protons and ions are in phase. The amplitude of the Alfvénic fluctuations in ions is smaller than the proton amplitude by a factor of $Z/A = 5/16$. The temporal variations in V_r of protons and ions (Figure 8) have global similarities. However, there are quantitative differences in the temporal variation due to different compressive effects in the proton and ion fluids. The driving source of the variations in V_r are nonlinear compressions due to the low-frequency Alfvén waves.

The corresponding density variations of protons and ions at $4R_\odot$ are shown in Figure 9.

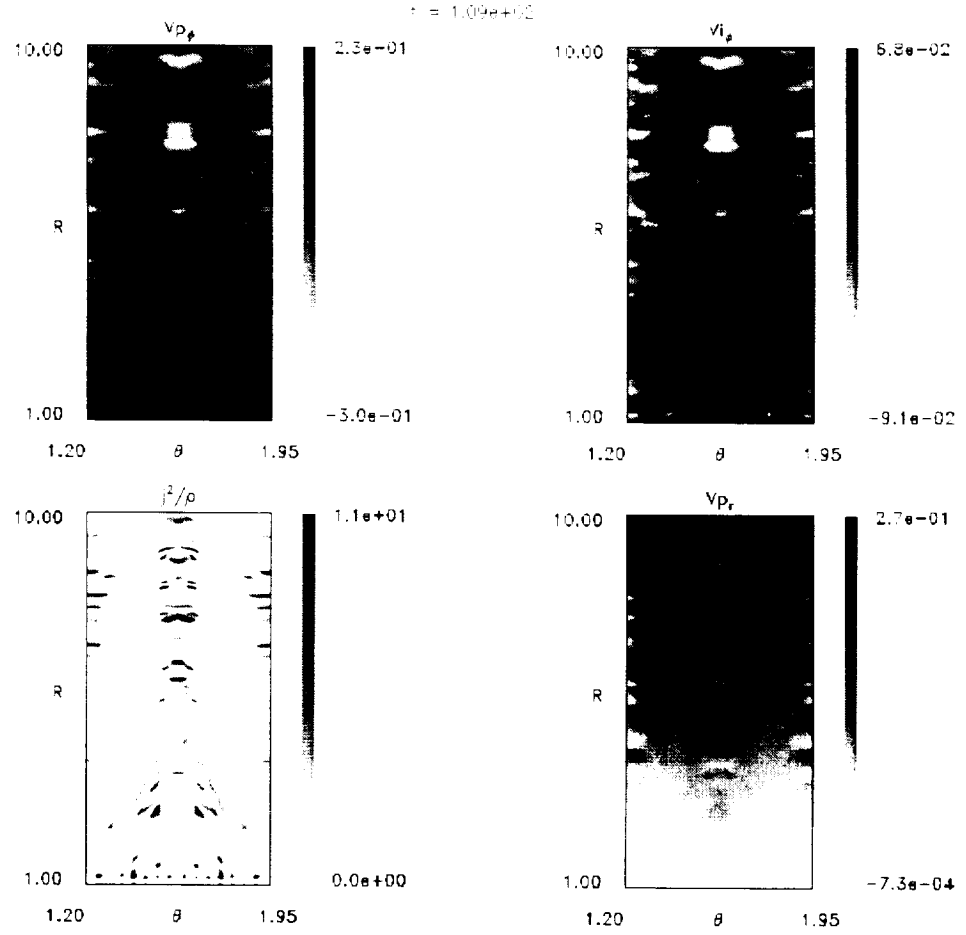


Fig. 7.— The spatial dependence of the ϕ -component of the proton and ion velocity, the Ohmic heating associated with the broad band Alfvén waves, and the radial velocity of the protons are shown. The velocities are scaled by $V_A = 1521 \text{ km s}^{-1}$.

It is evident that the density variations occur in phase with the radial velocity variations, as expected from compressive fluctuations. The slow increase in the average ion density is due to the diffusion of O^{5+} ions to larger heliocentric distances due to Coulomb friction. Using the faster 1D version of the code we have found that this process saturates after about $800\tau_A$. The time-averaged mass flux in the center of the model coronal hole at $4R_\odot$ is $2 \times 10^{-12} \text{ g cm}^{-2} \text{ s}^{-1}$, consistent with the mass flux at 1 AU determined from Ulysses data (Guhathakurta & Fisher 1998) for nearly radial expansion beyond $4R_\odot$.

In Figure 11 we show the radial dependence of the effective proton and O^{5+} temperature in the central (low density) region of the coronal hole. The effective temperatures were

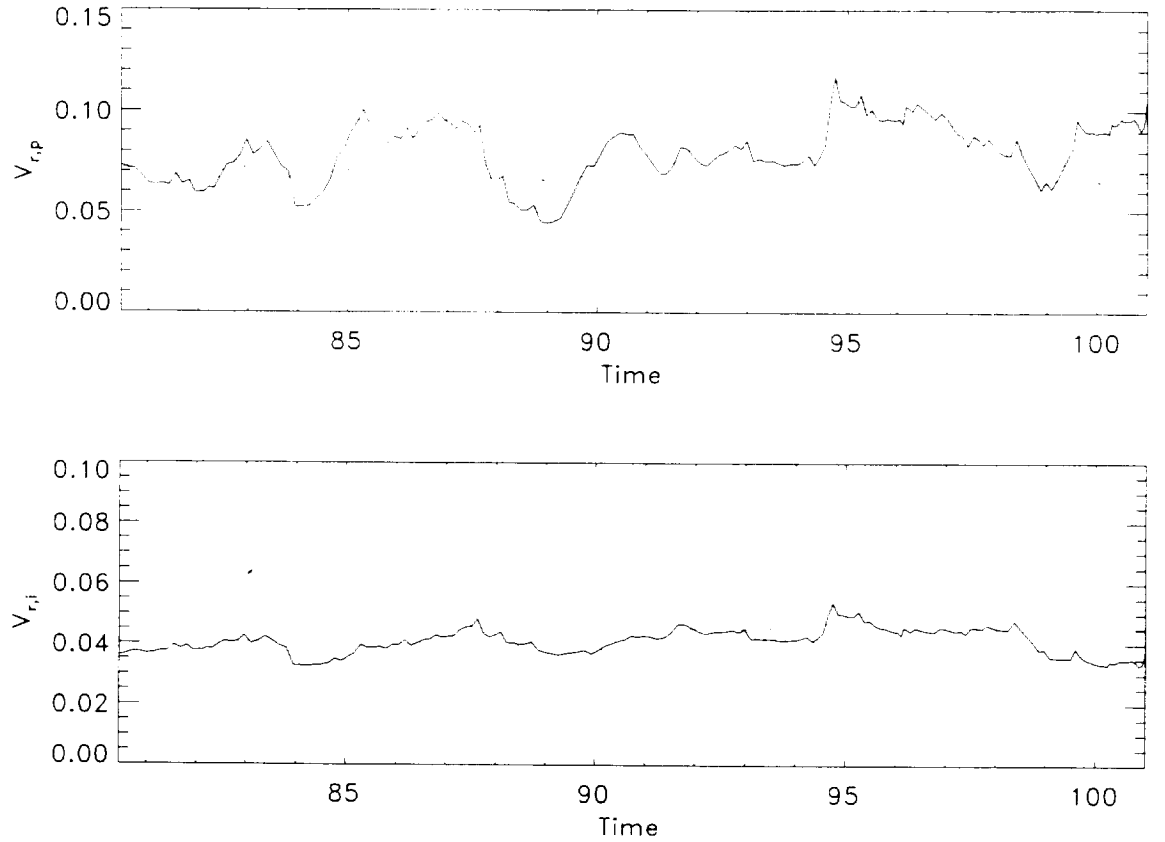


Fig. 8.-- The temporal evolution of the V_r of protons (top panel) and O^{5+} ions (bottom panel). The location is $r = 4R_{\odot}$ at $\theta = 1.58$ (solid line), 1.67 (short dashes), 1.76 (dashes), 1.85 (dot-dashes), 1.95 (3-dot-dashes). The velocities are scaled by $V_A = 1521 \text{ km s}^{-1}$, and the time is scaled by the Alfvén time, $\tau_A = 460 \text{ s}$.

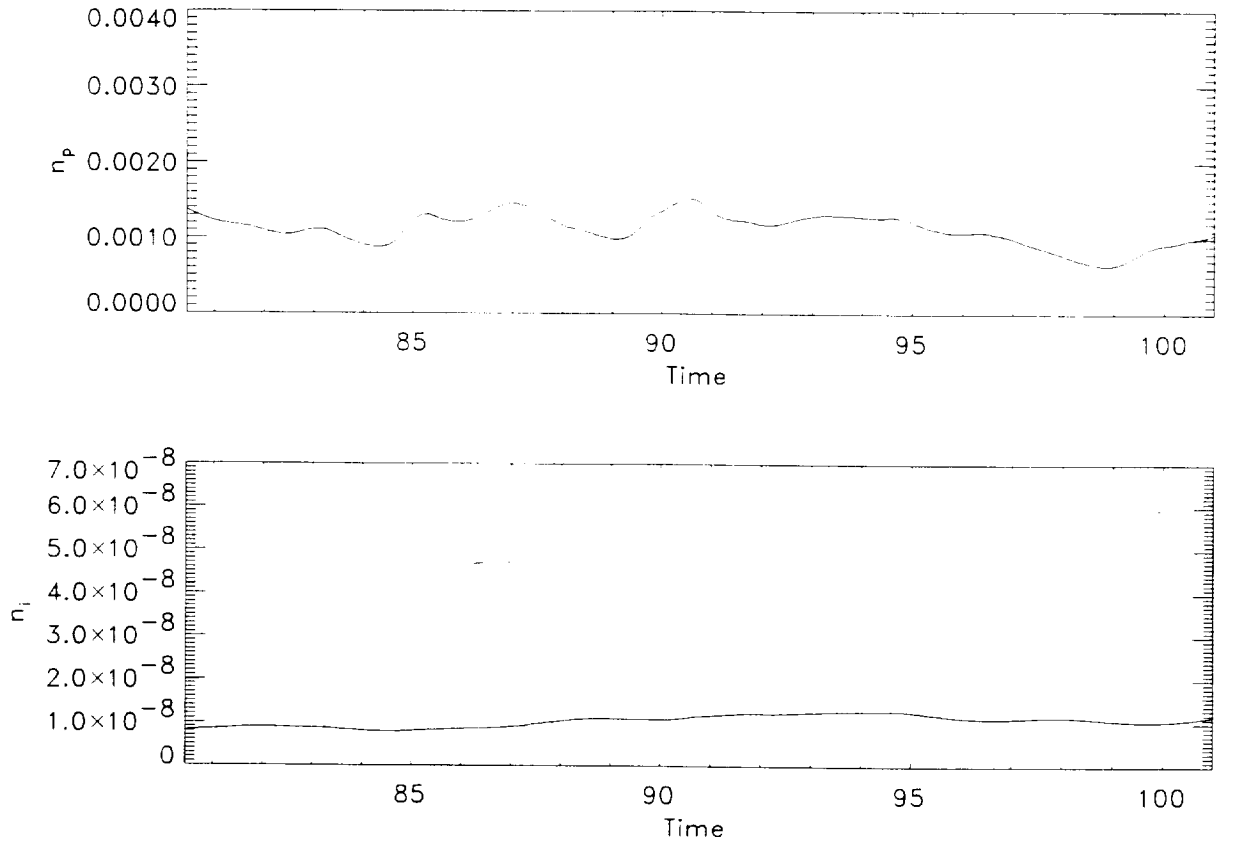


Fig. 9.— The temporal evolution of the proton density (top panel) and O^{5+} density (bottom panel). The location is $r = 4R_{\odot}$ at $\theta = 1.58$ (solid line), 1.67 (short dashes), 1.76 (dashes), 1.85 (dot-dashes), 1.95 (3-dot-dashes). The densities are scaled by $n_{e0} = 10^8 \text{ cm s}^{-3}$, and the time is scaled by the Alfvén time, $\tau_A = 460 \text{ s}$.

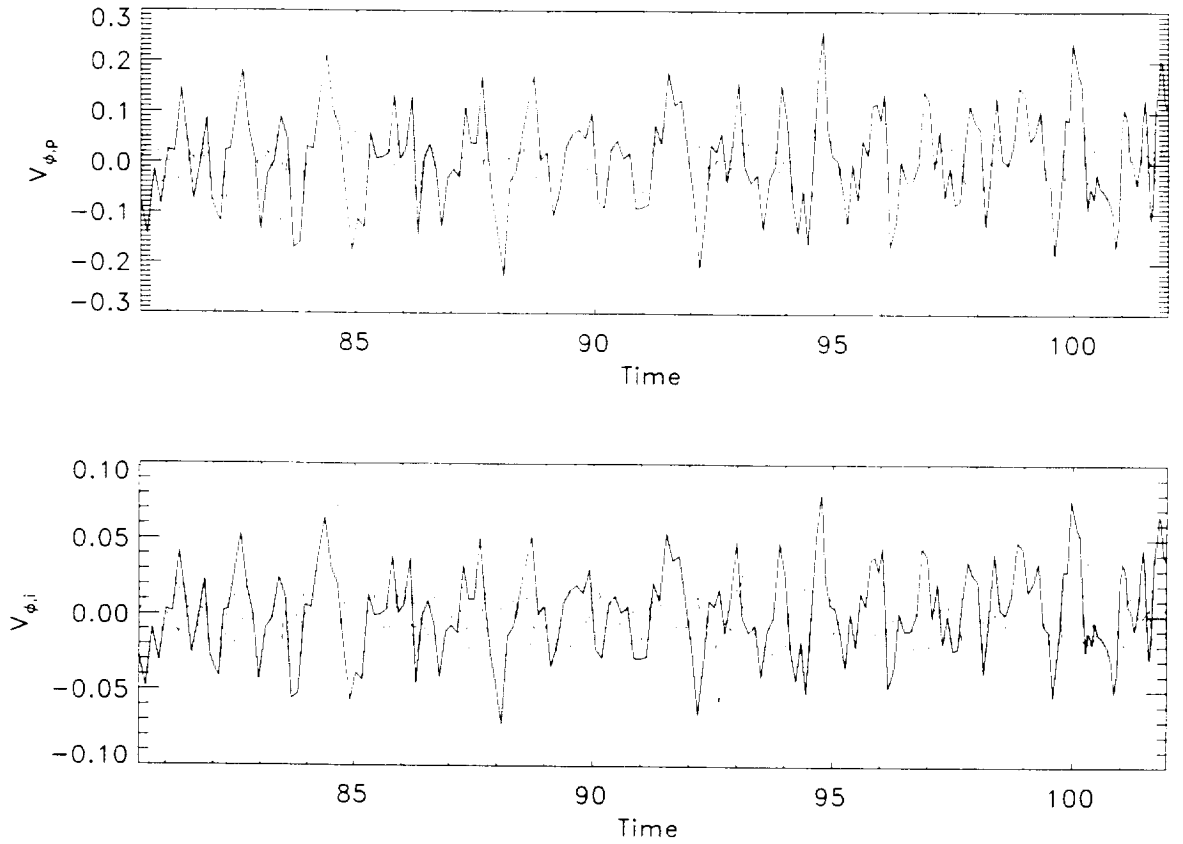


Fig. 10.— The temporal evolution of the V_ϕ of protons (top panel) and O^{5+} ions (bottom panel). The location is $r = 4R_\odot$ at $\theta = 1.58$ (solid line), 1.67 (short dashes), 1.76 (dashes), 1.85 (dot-dashes), 1.95 (3-dot-dashes). The velocities are scaled by $V_A = 1521 \text{ km s}^{-1}$, and the time is scaled by the Alfvén time, $\tau_A = 460 \text{ s}$.

obtained by integrating Equation (13) for protons and ions with the corresponding $\langle V_\phi(t) \rangle$. The velocities were averaged in time and in space (θ) to simulate the effects of 1.7 hour exposure of the UVCS observations. The dashed lines show the time-averaged kinetic temperature for the protons and ions that was obtained from the solution of the polytropic energy equation. The dotted line shows the electron temperature.

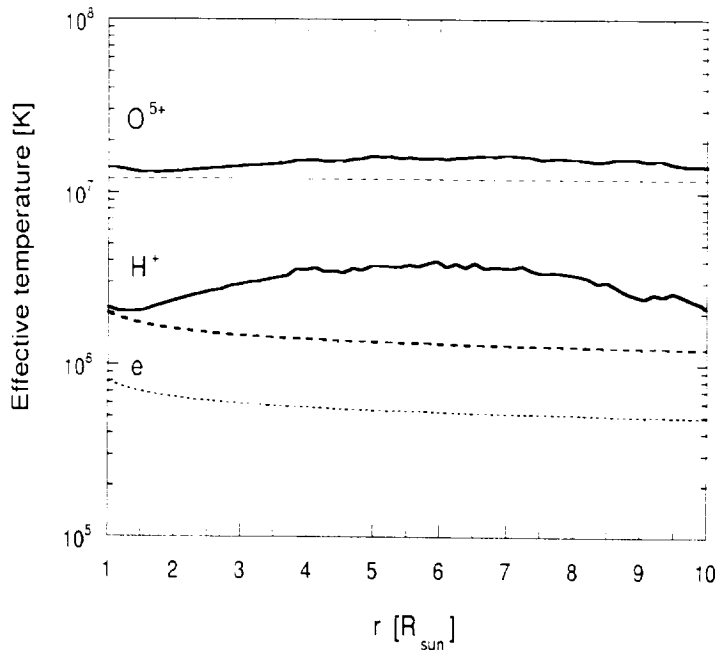


Fig. 11.— The effective temperatures (solid lines) due to unresolved wave motions for protons and O^{5+} ions obtained from the three-fluid model. The dashed lines are the time average temperatures obtained from the proton, ion, and electron polytropic energy equations in the model.

It is evident that the radial dependence of the effective proton temperature is in good qualitative agreement with UVCS observations (Kohl et al. 1997, Antonucci 1999). Due to the anisotropic velocity of the Alfvén waves the apparent peak proton anisotropy is $T_{eff}/T_p \approx 3$. However, the Alfvén waves can not explain the large perpendicular temperature of O^{5+} ions reported by UVCS (Kohl et al. 1997, Antonucci 1999). The effective O^{5+} temperature in the model is only about 50% larger than the kinetic temperature, and an order of magnitude smaller than the perpendicular temperature deduced from UVCS observations. As we have seen above the amplitude of the heavy ion response to the Alfvénic fluctuation is reduced by the smaller Lorenz force compared to the force on the protons. Coulomb friction does not affect significantly the amplitude of the perpendicular ion fluctuations. Due to the small collision frequency with the protons the

main effect of the Coulomb friction is to increase the average ion outflow speed and density on time-scales longer than the Alfvén wave period (Ofman 2000).

6. Constraints on the O^{5+} Anisotropy due to the Ion-Cyclotron Instability

In the present study we use linear kinetic theory and 1D hybrid simulations to constrain the possible ion anisotropy for typical coronal hole conditions close to the Sun. We investigate the relaxation of the O^{5+} ion temperature anisotropy for a range of ion parallel temperatures expected in a coronal hole. A 2-D hybrid code study of the anisotropic temperature oxygen ion instability with applications to the outer solar wind is in preparation (Gary et al. 2000).

We use the standard linear Vlasov theory for fluctuations and instabilities in a collisionless, homogeneous, magnetized plasma (Gary 1993). The protons and electrons are represented as Maxwellian velocity distributions, whereas the heavy ion species is a bi-Maxwellian with $T_{\perp i}/T_{\parallel i} > 1$. There are no average relative drifts between any two species, so the zero current condition is satisfied. Under these conditions, the fastest growing mode at sufficiently small $\beta_{\parallel i} = 8\pi n_e k_B T_{\parallel i}/B_0^2$ is the electromagnetic heavy ion cyclotron anisotropy instability (hereafter the “heavy ion cyclotron instability”), where n_e is the electron density, B_0 is the background magnetic field, and k_B is Boltzmann’s constant. The maximum growth rate is at $\mathbf{k} \times \mathbf{B}_0 = 0$; for this direction of propagation the linear properties of this mode are given by the dispersion equation stated in Gary and Lee (1994). We here present results from exact numerical solutions to this dispersion equation with no analytic approximations made for any species contribution. In each case we find that, on the given domain of $\beta_{\parallel i}$, the instability threshold condition can be fit to a curve of the form

$$\frac{T_{\perp i}}{T_{\parallel i}} - 1 = \frac{S_i}{[(m_p/m_i)\beta_{\parallel i}]^{\alpha_i}}. \quad (14)$$

The fitting parameter S_i changes with various parameters but is approximately of order unity, and $\alpha_i \sim 0.40$.

Figure 12 shows the threshold anisotropies for the oxygen ion cyclotron anisotropy instability as functions of the oxygen ion scaling parameter $(m_p/m_i)\beta_{\parallel i}$ for four different values of the normalized maximum growth rate γ_m/Ω_p , where Ω_p is the proton gyrofrequency. A stronger anisotropy corresponds to a faster growth rate, so although $\alpha_i \sim 0.4$ in each case, S_i increases as γ_m/Ω_p increases, just as S_p increases with maximum growth rate at the threshold of the proton cyclotron anisotropy instability (Gary & Lee 1994).

Other scalings of the linear instability threshold are not shown here, but may be

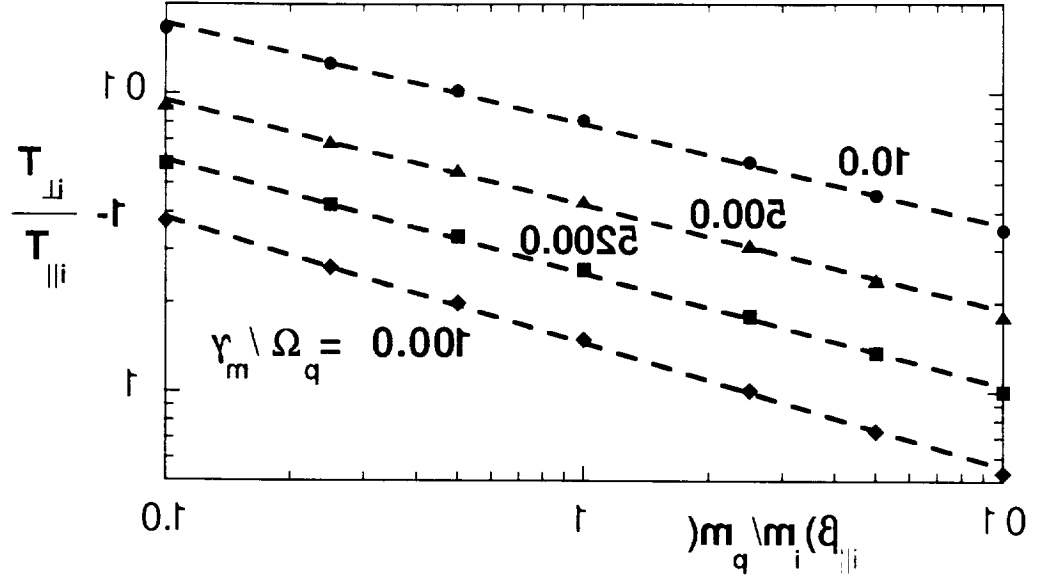


Fig. 12.— Linear Vlasov theory results. The oxygen ion temperature anisotropy at four different values of the maximum growth rate of the electromagnetic oxygen ion cyclotron anisotropy instability as a functions of the scaling parameter $(m_p/m_i)\beta_i$. Here the oxygen ions, O^{5+} , have $T_{\perp i}/T_{\parallel p} = 16.0$, $m_i/m_p = 16$, and $n_i/n_e = 0.0006$. The fitting parameters of Equation (14) are: at $\gamma_m/\Omega_p = 0.001$, $S_i = 1.46$ and $\alpha_i = 0.42$; at $\gamma_m/\Omega_p = 0.0025$, $S_i = 2.50$ and $\alpha_i = 0.38$; at $\gamma_m/\Omega_p = 0.0050$, $S_i = 4.23$ and $\alpha_i = 0.35$; and at $\gamma_m/\Omega_p = 0.010$, $S_i = 7.90$ and $\alpha_i = 0.34$.

summarized (under the assumption of $\gamma_m/\Omega_p = \text{constant}$) as follows: S_i generally decreases with increasing n_i/n_e and with increasing ionization state of the heavy ion (Gary et al. 2000). In contrast, the threshold does not change significantly as $T_{\perp i}/T_p$ is varied.

We are expanding our 2.5D MHD model into a full 3D description, which will allow to use more realistic model of a coronal hole and solar boundary conditions. For this purpose we are adapting our single fluid 3D MHD code and investigate various boundary conditions on the dynamics of waves in coronal magnetic structures (Ofman & Davila(2000)). Initially, we have developed the code on our SGI workstations. Next, the code has been parallelized by using the Message Passing Interface (MPI) to run on massively parallel computers, such as the T3E and on the Origin 2000. In the near future we plan to expand the code to model two- and three-fluid coronal plasma dynamics.

7. Hybrid Numerical Simulations of the 3-component Plasma

We use a one-dimensional hybrid code (Harned 1982, Terasawa et al. 1986, Winske & Omidi 1993, Agim, Viñas, & Goldstein 1995) to model a collisionless, homogeneous, magnetized plasma. In the hybrid model the ions are represented as particles, while the electrons are described as a massless fluid to maintain quasineutrality of the plasma. This method allows one to resolve the ion dynamics and to integrate the equations over many ion-cyclotron periods, while neglecting the small time- and spatial- scales of the electron kinetic motions. The particle and field equations are integrated in time using a rational Runge-Kutta method whereas the spatial derivatives are calculated by pseudospectral FFT method.

The electrons are represented as a massless fluid having zero average flow speed. There are no initial relative drifts among the species. We use a periodic system in x with the background magnetic field $\mathbf{B}_0 = \hat{x}B_0$. We have used 256 grid cells to solve for the fields, with 100 particles per cell for each component and with grid size $dx = 1.5$ in units of proton inertial length, c/ω_{pp} , where c is the speed of light, and ω_{pp} is the proton plasma frequency. The system dimension L approximately equals four times the wavelength of the fastest growing mode. The integration time step was $\Omega_p \Delta t = 0.05$.

We use the empirical values of the coronal parameters at $3.5R_\odot$ reported by Cranmer et al. (1999): $n_e = 3.55 \times 10^4 \text{ cm}^{-3}$, $T_e = 7.2 \times 10^5 \text{ K}$, $T_{\parallel p} = 1.4 \times 10^6 \text{ K}$. We assume that $B_0(1R_\odot) = 5 \text{ G}$, and get $B_0(3.5R_\odot) = 0.0655 \text{ G}$ and $\Omega_p = 6.3 \times 10^2 \text{ Rad s}^{-1}$. In this study we also assume that initially $T_{\perp p} = T_{\parallel p}$. Thus, we initialize the protons as a single isotropic Maxwellian velocity distribution, whereas the heavy ion species are initially a bi-Maxwellian with $T_{\perp i}/T_{\parallel i} = 50$.

The abundance of O^{5+} relative to protons in the corona at $3.5R_\odot$ is about 8×10^{-6} (Wimmer-Schweingruber et al. 1998). Due to numerical limitations we are using higher abundance of 6×10^{-4} . We have performed test runs with the coronal O^{5+} abundance, which requires much higher resolution, larger number of particles, and longer computation times, and found qualitatively similar results, with somewhat longer relaxation time and higher final anisotropy. To reduce the abundance to coronal values will require numerical effort beyond the scope of this study.

We initiated the hybrid simulation with $T_{\parallel i} = T_{\parallel p} = 1.4 \times 10^6 \text{ K}$, which corresponds to $\beta_{\parallel i} = 0.0413$ (we vary $\beta_{\parallel i}$ below). We have run the simulation until the O^{5+} anisotropy reached a quasi-steady state with final $\beta_{\parallel i} = 0.143$. The $\beta_{\parallel i}$ has increased due to the transfer of kinetic energy from the perpendicular to parallel direction of the ions. In Figure 13 we show the anisotropy of O^{5+} as a function of time. It is evident that the relaxation occurs in

$t_{rel} \approx 900\Omega_p^{-1}$. The anisotropy exhibits two main stages of evolution: (1) rapid relaxation on a typical timescale t_{rel} ; (b) slow decrease to an asymptotic value.

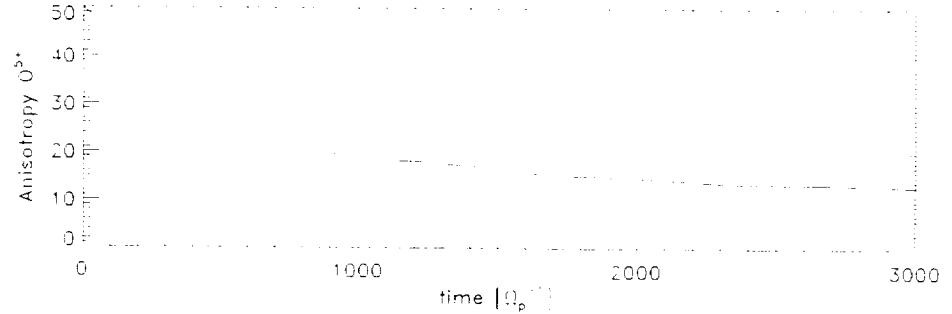


Fig. 13. --- The temporal evolution of the O^{5+} ion temperature anisotropy for typical coronal hole conditions. The initial parallel temperature was set to $T_{\parallel i} = T_{\parallel p} = 1.4 \times 10^6$ K, which corresponds to $\beta_{\parallel i} = 0.0413$. The final $\beta_{\parallel i} = 0.143$.

The rapid stage is characterized by an increase of the magnetic fluctuations evident in Figure 14. The increase of $|\delta\mathbf{B}/\mathbf{B}|^2$ is on the same timescale t_{rel} as the relaxation of the anisotropy. The linear stage of the instability corresponds to an exponential growth of the magnetic perturbation. The average magnetic perturbation grows exponentially during the first 900 proton cyclotron periods, following an onset period of 300 proton cyclotron periods. At later times the instability nonlinearly saturates. The magnetic fluctuation includes contribution from all unstable modes, with the dominant contribution from the fastest growing mode.

In Figure 15 we show the velocity distribution of O^{5+} in the simulation at the end of the run in Figure 13. The distribution of $V_{x,i}$ (long dashes), $V_{y,i}$ (solid line), and $V_{z,i}$ (short dashes) is shown. The dotted line is the corresponding Maxwellian. The $V_{x,i}$ is parallel, and the $V_{y,i}$ and $V_{z,i}$ are perpendicular to the background magnetic field. It is evident that the anisotropic distribution of the O^{5+} velocity is close to bi-Maxwellian with the perpendicular component broader than the parallel in agreement with the anisotropy at the end of the run in Figure 13. The fluctuations in the distributions due to the statistical noise do not significantly affect the results.

The relaxation of the anisotropy and the increase of the magnetic fluctuation occur due to the ion-cyclotron instability that develops in the O^{5+} . The rapid phase corresponds to the exponential growth phase of the instability, while during the asymptotic relaxation stage the instability has nonlinearly saturated. Linear Vlasov theory, and nonlinear particle and hybrid simulations show that in collisionless plasma the relaxed velocity distribution



Fig. 14.— The temporal evolution of the perturbed relative magnetic field fluctuation $|\delta\mathbf{B}/\mathbf{B}|^2$ generated by the ion-cyclotron instability of the O^{5+} ions. To remove statistical high-frequency noise a running average smoothing was applied to this quantity. Note, that the saturation time of the fluctuations corresponds to the relaxation time of the ion anisotropy.

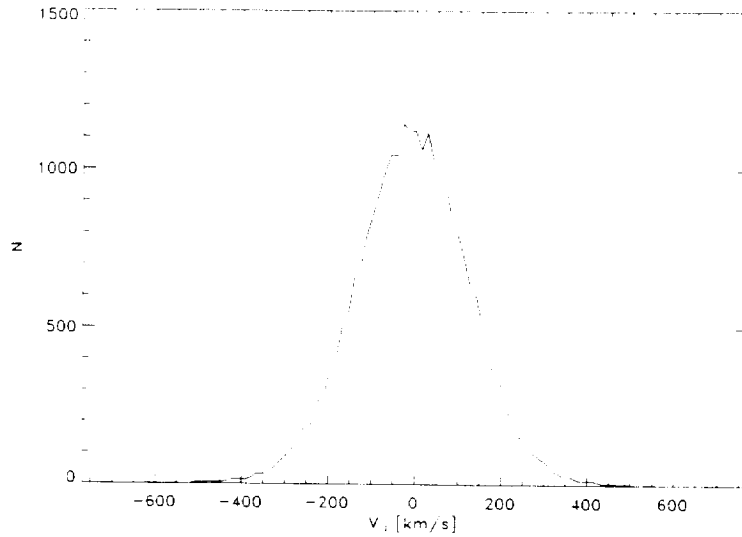


Fig. 15.— The velocity distribution of O^{5+} in the simulation at the end of the run of Figure 13. The distribution of $V_{x,i}$ (long dashes), $V_{y,i}$ (solid line), and $V_{z,i}$ (short dashes) are shown (N is the number of the particles). The dotted line is the corresponding Maxwellian.

does not return to a fully isotropic condition (Cuperman, Ofman, & Dryer 1986, Gary et al. 2000).

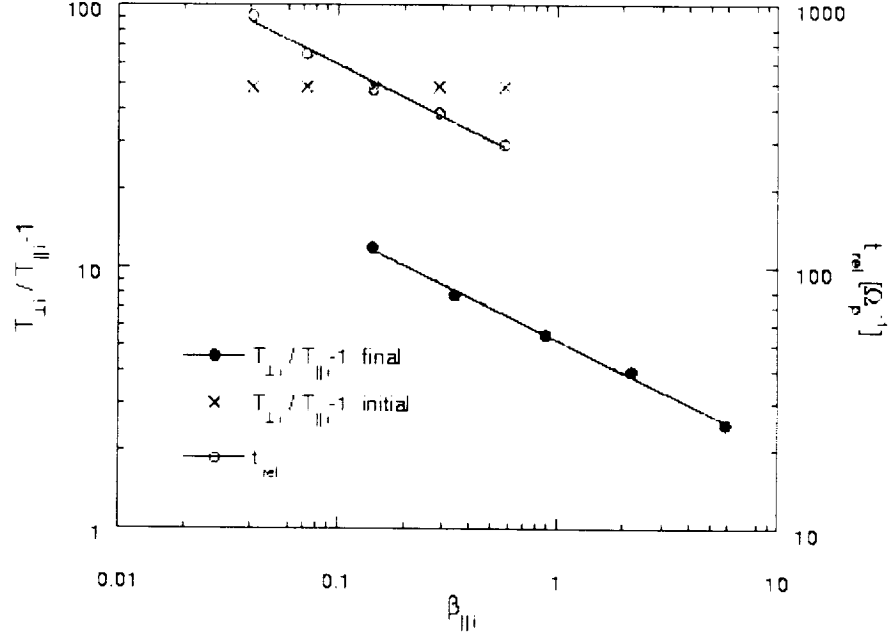


Fig. 16.— The results of the parametric study of the hybrid simulation. The scaling of the relaxed $T_{\perp i}/T_{\parallel i} - 1$ with the final $\beta_{\parallel i}$ (full circles). The scaling of the relaxation time, t_{rel} , with the initial $\beta_{\parallel i}$ (circles). Both quantities scale as $\beta_{\parallel i}^{-0.41}$. The “x”’s mark the values $T_{\perp i}/T_{\parallel i} - 1$ at $t=0$.

In Figure 16 we show the dependence of t_{rel} and the relaxed anisotropy on $\beta_{\parallel i}$. In this study we have varied the initial $\beta_{\parallel i}$ in the range 0.041-0.577. This corresponds to $T_{\parallel i}$ in the range $(1.4 - 20.0) \times 10^6$ K. We found that t_{rel} and the final $T_{\perp i}/T_{\parallel i} - 1$ scale as $\beta_{\parallel i}^{-0.41}$ in agreement with the linear theory (Equation 14). Note, that we plot the scaling of t_{rel} with the initial $\beta_{\parallel i}$, while the scaling of $T_{\perp i}/T_{\parallel i} - 1$ is with the final $\beta_{\parallel i}$. The “x”’s denote the anisotropy at $t=0$ for each case. We find that decreasing the initial $T_{\parallel i}$ leads to larger final anisotropy of the O^{5+} , and to longer relaxation times that correspond to smaller growth rate of the ion-cyclotron instability.

8. Analysis

We developed the three-fluid 2.5D MHD numerical model to investigate the acceleration of the slow and fast solar wind, and the effect of waves on protons and minor ions. According to this model the main mechanism responsible for the observed structure of streamers in O^{5+} is the Coulomb friction between the O^{5+} ions and the outflowing protons. The friction leads to the increase in the density and the outflow speed of the minor ions in the open field regions. The same qualitative enhancement is expected for Fe^{11+} and other minor ions in these regions. In order to verify that the Coulomb friction is the physical mechanism that leads to the enhanced O^{5+} abundance in streamer legs we have repeated the above calculation without the Coulomb friction terms, and found much smaller abundance enhancement of O^{5+} (order of few percent) in the legs of streamers, and an order of magnitude smaller O^{5+} outflow speed in the open field regions. Other possible mechanism that may contribute to the enhanced O^{5+} abundance in the legs of streamers are preferential heating of the ions in these regions, and variations in the ion abundance at the coronal boundary of the legs. These possibilities are left for future studies.

Based on these results, and on recent SOHO/UVCS observations of the solar wind in solar coronal streamers we conclude that the observed enhanced minor ion emission in the legs of streamers is the signature of the slow solar wind outflow regions. The identification of these regions allows to trace the slow solar wind sources low above the limb, and into the extended corona. This will help to understand the origins and the composition of the slow solar wind, and the effect on the interplanetary environment. Using the three-fluid 2.5D MHD model we study the role of broad-band low frequency MHD waves and coronal structures on the EUV line profiles. We calculate the apparent proton and ion temperatures from the simulated EUV emission lines. We find that for reasonable coronal parameters and Alfvén wave spectrum (i.e., consistent with nonthermal line broadening near the limb) the wave motions in the line of sight can account for the observed Ly- α line broadening, but can not explain the broad OVI lines.

We find with our three-fluid model that the UVCS observations of broad Ly- α lines suggest the presence of low-frequency Alfvén wave in coronal holes that are responsible for the enhanced proton temperature and anisotropy. Thus, these waves accelerate the protons in coronal holes in agreement with our earlier single fluid models (Ofman & Davila 1997a, Ofman & Davila 1997b, Ofman & Davila 1998). Our three-fluid model suggest that the observed increase of the line-width proton temperature is due to temporally and spatially unresolved low-frequency wave motions of the protons. Thus, the MHD waves may contain a significant fraction of the solar wind energy in the lower corona, and therefore, may play an important role in the acceleration and heating of the fast solar wind.

However, the low frequency Alfvén wave spectrum can not produce the broad O^{5+} lines observed by the UVCS. According to the three-fluid model the perpendicular O^{5+} velocities are about factor of 5 smaller than the velocities reported by Kohl et al. (1997). Due to the low abundance, low collision rate, and low charge to mass ratio of the O^{5+} ions compared to protons it is possible that high frequency waves play a more important role in heating these ions than in proton heating. Thus, resonant absorption of ion-cyclotron waves, may be responsible for the high minor ion temperature and anisotropy deduced from UVCS observations in agreement with other studies (e.g., Cranmer, Field, & Kohl 1999, Ofman, Viñas, & Gary 2001).

We find that the large O^{5+} ion anisotropy deduced from UVCS observations is unstable to an electromagnetic ion-cyclotron instability. We use the scaling law for instability threshold obtained from linear Vlasov theory to relate the heavy ion temperature anisotropy to the parallel heavy ion beta. The linear theory relies on the assumption that the ion distribution function is bi-Maxwellian, which is reasonable for the inner corona. Obviously, the linear theory does not account for the self-consistent interaction between the waves and the particles, and the saturation of the instability.

The hybrid simulation allows the self-consistent evolution of the velocity distribution of the ions (e.g., bi-Maxwellian distribution is not imposed at $t > 0$). It includes the nonlinear self-consistent description of the wave-particle interaction, and the nonlinear saturation of the instability. The simulations show that these nonlinear effects constrain the values of the ion anisotropy for a range of coronal parameters. Furthermore, the simulated constraint is in agreement with the instability threshold scaling derived from linear theory.

For typical coronal hole conditions at $3.5R_{\odot}$ and isotropic protons, an initial O^{5+} anisotropy of 50 decreases by an order of magnitude within ~ 300 -900 proton cyclotron periods (3-9 s for coronal values of B). The relaxation time and the final anisotropy decreases when the initial $T_{\parallel i}$ is increased. Thus, in order to sustain the anisotropy of 50 the O^{5+} ions must be heated and the resonating ion-cyclotron wave spectrum must be produced on these timescales. The results of this study are applicable to the future *Solar Probe* in-situ velocity distribution observations close to the Sun.

REFERENCES

- Agim, Y. Z., A. F. Viñas, & M. L. Goldstein 1995, *J. Geophys. Res.*, 100, 17081
 Alazraki, G., & Courtier, P. 1971, *A&A*, 13, 380
 Anders, E. & Grevesse, N. 1989, *Geochim. Cosmochim. Acta*, 53, 197
 Antonucci, E. 1999, *Proceedings 8th SOHO Workshop*, ESA SP-446, 53
 Athay, R.G., & White, O.R. 1979, *ApJS*, 39,333

- Axford, W. I. & McKenzie, J. F. 1992. Solar Wind Seven Colloquium. 1
- Belcher, J.W. 1971. ApJ. 168, 509
- Braginskii, S. I. 1965. Rev. Plasma Phys., 1, 205
- Bürgi, A., & Geiss, J. 1986. Solar Phys., 103, 347
- Cranmer, S., Field, G.B., & Kohl, J.L. 1999. Astrophys. J., 518, 937
- Cuperman, S., Ofman, L., & Dryer, M. 1986. J. Plas. Phys., 36, 387
- Cuperman, S., Ofman, L., Dryer, M. 1990. ApJ, 350, 846
- Davila, J.M., Ofman, L. 1999, Sp. Sci. Rev., 87, 287
- Dusenbery, P. B. & Hollweg, J. V. 1981. J. Geophys. Res., 86, 153
- Esser, R., & Leer, E. 1990, J. Geophys. Res., 95, 10269
- Gary, S.P., et al. 2001. in press
- Guhathakurta, M. & Fisher, R. 1998, ApJ, 499, L215
- Gary, S.P. 1993. Theory of Space Plasma Microinstabilities. Cambridge Univ. Press, New York
- Gary, S.P., Lee, M.A. 1994. J. Geophys. Res., 99, 11297
- Geiss, J., Hirt, P., & Entwyler, H., Solar Phys., 12, 458
- Harned, D. S. 1982. J. Comp. Phys., 47, 452
- Joselyn & Holzer 1978. J. Geophys. Res., 83, 1019
- Kohl, J.L. et al. 1997, Sol. Phys., 175, 613
- Li X., et al. 1997. J. Geophys. Res., 102, 17419
- Li, J., J. C. Raymond, L. W. Acton, et al. 1998, ApJ, 506, 431
- McKenzie, J. F. & Marsch, E. 1982. Astrophysics and Space Science, 81, 295
- Noci, G. et al. 1997. Fifth SOHO Workshop: The Corona and Solar Wind Near Minimum Activity, ESA, SP-404, 75
- Ofman, L. 2000, Geophys. Res. Lett., 27, 2885
- Ofman, L., & Davila, J.M., 1997a, Astrophys. J., 476, 357
- Ofman, L., & Davila, J.M., 1997b, Astrophys. J., 476, L51
- Ofman, L., Davila, J.M., 1998, 103, 23677.
- Ofman, L., Davila, J.M. 1999, Solar Wind Nine, S. Habbal et al. (eds). AIP Conference Proceedings, 471, 405-408. AIP, New York
- Ofman, L. & Davila, J. M. 2000. AAS/Solar Physics Division Meeting, 32, 604
- Ofman, L., Viñas, A., & Gary, S.P., 2001, ApJ, 547, L175
- Parker, E.N. 1963, Interplanetary Dynamical Processes, New York, Interscience
- Pneuman, G.W., and Kopp, R.A. 1971, Sol. Phys., 18, 258
- Raymond, J. C., et al. 1997, Sol. Phys., 175, 645
- Raymond, J. C., et al. 1997, Proc. 31st ESLAB Symp., ESA publ. SP-415, 383, ESA Publications Div., Noordwijk, The Netherlands
- Sittler, E.C., et al. 1997, in AIP Conf. Proc. 385, Robotic Exploration Close to the Sun: Scientific Basis, ed. S.R. Habbal (Woodbury: AIP), 59
- Steinolfson, R.S., Wu, S.T., Suess, S.T. 1982, ApJ, 255, 730
- Strachan, L., et al. 2000. J. Geophys. Res., 105, 2345
- Terasawa, T., M. Hoshino, J.-I. Sakai, & T. Hada 1986, J. Geophys. Res., 91, 4171

- Wang, A.-H. et al. 1993. *Sol. Phys.*, 147, 55
- Washimi, H., Yoshino, Y., Ogino, T. 1987. *Geophys. Res. Lett.*, 14, 487
- Wimmer-Schweingruber, R. F., et al. 1998. *Space Science Reviews*, 85, 387
- Winske, D. and Omid, N. 1993. in *Computer Space Plasma Physics: Simulation Techniques and Software*, ed. H. Matsumoto and Y. Omura. Terra Scientific Publishing, p. 103. 1993.

9. Publications

Below is the list of publications that were supported in full or in part by this contract in the period covered by this report.

1. Airapetian, V.S., Ofman, L., Robinson, R.D., Carpenter, K.G., Davila, J.M., Two-Component Winds from Luminous Late-type Stars. *The Astrophysical Journal*, *528*, 965, 2000.
2. Nakariakov, V.M., Ofman, L., Arber, T.D., Nonlinear Dissipative Spherical Alfvén Waves in Solar Coronal Holes, *Astronomy and Astrophysics*, *353*, 741, 2000.
3. Ofman, L., Nakariakov, V.M., Sehgal, N., Dissipation of Slow Magnetosonic Waves in Coronal Plumes. *The Astrophysical Journal*, *533*, 1071, 2000.
4. Ofman, L., Source Regions of the Slow Solar Wind in Coronal Streamers. *Geophysical Research Letters*, *27*, 2885, 2000.
5. Ofman, L., Propagation and Dissipation of Slow Magnetosonic Waves in Coronal Plumes. Last Total Solar Eclipse of the Millennium. W. Livingston and A. Ozguc (eds.), *PASP*, *205*, 147, 2000.
6. Ofman, L., Three-fluid 2.5D MHD models of waves in solar coronal holes and the relation to SOHO/UVCS observations, *Waves in Dusty, Solar and Space Plasmas*. F. Verheest et al. (eds.), *AIP Conference Proceedings*, *537*, pp. 119-125, AIP, New York, 2000.
7. Ofman, L., Viñas, A., Gary, S.P., Constraints on the O^{5+} Anisotropy in the Solar Corona, *The Astrophysical Journal Letters*, *547*, L175, 2001.
8. Gary, S.P., Yin, L., Winske, D., and Ofman, L., Electromagnetic Heavy Ion Cyclotron Instability: Anisotropy Constraint in the Solar Corona, *Journal of Geophysical Research*, 2001, in press.
9. Ofman, L., Davila, J.M., Three-fluid 2.5D MHD Model of the Effective Temperature in Coronal Holes, *The Astrophysical Journal*, 2001, in press.
10. Nakariakov, V.M., Ofman, L., Determination of the coronal magnetic field by coronal loop oscillations, *Astronomy and Astrophysics*, 2001, submitted.

1. REPORT NO.	2. GOVERNMENT ACCESSION NO.	3. RECIPIENT'S CATALOG NO.
4. TITLE AND SUBTITLE Acceleration of the Fast Solar Wind by Solitary Waves in Coronal Holes		5. REPORT DATE CODE:
7. AUTHOR(S) Dr. Leon Ofman		8. PERFORMING ORGANIZA- TION REPORT NO:
9. PERFORMING ORGANIZATION NAME AND ADDRESS Raytheon ITSS Corporation 4400 Forbes Blvd. Lanham, MD 20706		10. WORK UNIT NO. 11. CONTRACT OR GRANT NO. NASW-98004
12. SPONSORING AGENCY NAME AND ADDRESS Solar Physics Branch Code SS NASA Headquarters Washington, DC 20546		13. TYPE OF REPORT AND PERIOD COVERED Final progress report: 12 February 2000 - 11 February 2001
15. SUPPLEMENTARY NOTES		14. SPONSORING AGENCY CODE NASA HQ/ CODE SS
16. ABSTRACT The purpose of this investigation is to develop a new model for the acceleration of the fast solar wind by nonlinear, time-dependent multidimensional MHD simulations of waves in solar coronal holes. Preliminary computational studies indicate that solitary-like waves are generated in coronal holes nonlinearly by torsional Alfvén waves. These waves in addition to thermal conduction may contribute considerably to the accelerate the solar wind. Specific goals of this proposal are to investigate the generation of nonlinear solitary-like waves and their effect on solar wind acceleration by numerical 2.5D MHD simulation of coronal holes with a broad range of plasma and wave parameters; to study the effect of random disturbances at the base of a solar coronal hole on the fast solar wind acceleration with a more advanced 2.5D MHD model and to compare the results with the available observations; to extend the study to a full 3D MHD simulation of fast solar wind acceleration with a more realistic model of a coronal hole and solar boundary conditions. The ultimate goal of the three year study is to model the fast solar wind in a coronal hole, based on realistic boundary conditions in a coronal hole near the Sun, and the coronal hole structure (i.e., density, temperature, and magnetic field geometry) that will become available from the recently launched SOHO spacecraft.		
17. KEY WORDS (SUGGESTED BY AUTHOR(S)) Solar Wind Corona, MHD, Coronal Holes		18. DISTRIBUTION STATEMENT Space Science, Solar Physics
19. SECURITY CLASSIF. None	20. SECURITY CLASSIF. None	21. NO OF PAGES 22. PRICE